Journal of The Electrochemical Society, **157** (6) D357-D369 (2010)
0013-4651/2010/157(6)/D357/13/$28.00 © The Electrochemical Society

Impact of Accompanying Hydrogen Generation on Metal Nanotube Electrodeposition

Munekazu Motoyama,[a,*] Yasuhiro Fukunaka,[c,*,z] Yukio H. Ogata,[d,*] and Friedrich B. Prinz[a,b,*]

[a]*Department of Mechanical Engineering and* [b]*Materials Science and Engineering, Stanford University, Stanford, California 94305, USA*
[c]*Graduate School of Energy Science, Kyoto University, Kyoto 606-8501, Japan*
[d]*Institute of Advanced Energy, Kyoto University, Kyoto 611-0011, Japan*

Ni is electrodeposited into polycarbonate porous membrane templates at various cathodic potentials and bulk solution pH values. The membrane pore diameters are 200 nm. Transmission electron microscope observations reveal that the electrodeposited Ni nanostructures are nanowires but occasionally nanotubes. The nanotube wall thicknesses vary from 10 to 70 nm. Nanotubes with thinner walls are deposited under more acidic and less noble conditions. The numerical model for pH values at the cathode surface in the template is developed. Calculated pH values at the cathode surface are lower in the template than those at a vertical planar cathode. The current efficiency of Ni is measured by inductively coupled plasma emission spectrometry. As the predicted by the pH calculations, the current efficiency of Ni is lower for a porous template than for a vertical planar cathode. The observed nanotube walls become thinner as the current efficiency decreases. Thus, it is deduced that accompanying H_2 evolutions promote nanotube growth in the pores. Finally, the pH values in the template are more than 1 to 2 times smaller than at the vertical planar cathode surface.
 [DOI: 10.1149/1.3365038]

Manuscript submitted June 22, 2009; revised manuscript received February 22, 2010. Published May 3, 2010.

Electrochemical deposition in porous, thin-film-like polycarbonate membranes and anodized alumina films, as a technique to produce one-dimensional (1D) inorganic nanostructures such as metallic nanowires and nanotubes, has attracted a great deal of interest.[1-9] Many authors have investigated the physical properties and crystallographic characterization of the produced nanostructures with scientific interest and with a goal of applying them to various functional nanodevices, such as magnetic recording media,[1-4] energy conversion electrodes,[5,6] and chemical sensors.[7-9] Occasional observations of hollow tube growth in the templates have interested several authors.[10-17] In comparison to metallic nanowires, metallic nanotubes exhibit higher surface-to-volume ratios.[18,19] The possibility of nanotubes serving as channels for molecular selection and delivery[20] and the capability toward realizing unique magnetic configurations unattainable in magnetic wires[21] make metallic nanotubes attractive for a wide range of future applications. However, it is still unclear as to what exactly occurs during the electrodeposition process of nanotubes in the finite-sized pores enclosed by polymer or ceramic walls.

Various growth models have been suggested. Tourillon et al. reported that Fe and Co nanotubes were deposited by a pulsed potentiostatic method.[10,11] In a polycarbonate membrane, they observed that scheduling cycles of a short plating time followed by a long off time produced nanotubes. They consider that the surface carbonate groups of membrane walls induce complexation with metal ions. Hence, metallic adatom layers form on the surfaces, and the electrodeposition on the adatom layers subsequently increases the tube wall thicknesses. Metal nanotubes were successfully produced by chemically modifying the template walls to catalyze metal deposition on the wall surfaces.[22-24]

However, Tourillon et al.'s model was not sufficient to explain the electrodeposition processes of nanotubes under various conditions encountered in the subsequent literature. Continuous constant currents[12-14] and potentials[15-17] can also grow Au, Cu, Fe, Co, and Ni nanotubes in polycarbonate membranes and anodized alumina films. Moreover, electrolyte compositions,[15-17] cathode geometry at the template bottom,[12,16] and the kind of organic additive used[14] are also critical. Hence, a clear understanding of electrochemical nanotube growth has not yet been found, although improved insights promise better strategies in designing and building next-generation nanostructures.

Fukunaka et al. investigated the effects of cathodic potential and electrolyte pH on Ni nanostructures electrodeposited in polycarbonate templates.[15] They reported that when the cathodic potential was more positive or the electrolyte pH was lower, the deposited structures tended to form hollow tubes. Moreover, the tube wall thicknesses varied from 10 to 70 nm, with an outer diameter of 200 nm, depending on the cathodic potential and pH. Tube wall thicknesses that are controllable over a wide range of internal radii may offer interesting scientific opportunities. Ni plays catalytic roles in various (electro)chemical processes such as the anode reaction of a solid oxide fuel cell,[25,26] hydrogen production by methane decomposition,[27] and growth of carbon nanotubes.[28] Moreover, the range of applications is further broadened by the fact that metal nanotubes may be deposited from many different materials.

Fukunaka et al. presumed that the hollow core of a Ni nanotube is associated with a H_2 nanobubble because a lower pH electrolyte produces more significant H_2 generation.[29,30] In their model, an electrochemically growing nanotube traps a nucleated H_2 bubble in the center of the end. The bubble neither escapes nor disappears because H_2 gas molecules are continuously generated at the peripheral edge of the tube during the deposition and diffuse to the larger H_2 bubble in the core before nucleating multiple bubbles there. However, the inner pressures of the nanobubble were so high (Young–Laplace equation) that the gas solubility in the solution was increased at the front face of the bubble (Henry's law). The balance between the absorption and dissolution rates of the H_2 molecules stabilized the H_2 gas/aqueous electrolyte interface of the nanobubble. The inner diameter of the nanotubes is determined by the size of a bubble present in the center. The literature also pointed out the critical role of H_2 evolution in nanotube growth.[16,17] To understand the electrodeposition process of the nanotubes, measurements of H_2 evolution rates are indispensable.

Our study aims to measure the current efficiency of Ni electrodeposition in polycarbonate membrane templates by inductively coupled plasma (ICP) emission spectrometry. We use the calculation model to estimate the ionic species concentration at the cathode surface in the nanoporous template. The calculated results show that the pH value at the cathode surface in the template is much lower when compared to a vertical planar cathode. From the results of a vertical planar cathode, the measured current efficiency of Ni is

* Electrochemical Society Active Member.
z E-mail: fukunaka@energy.kyoto-u.ac.jp

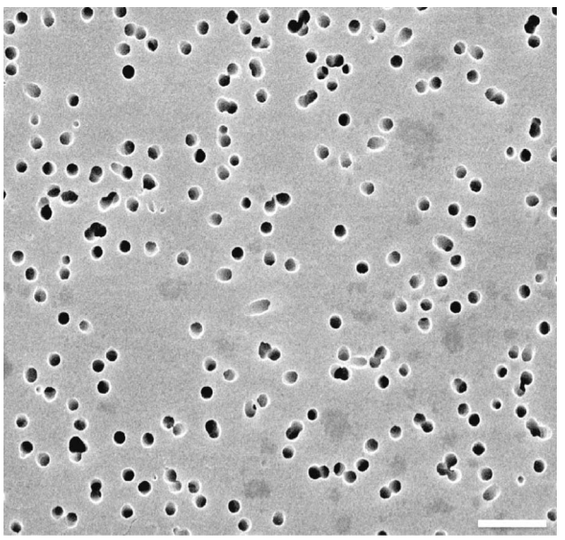

Figure 1. SEM image of a polycarbonate-track-etched membrane surface after sputter deposition of a 30 nm thick Pt–Pd alloy layer. The nominal diameter of the pores is 200 nm. Scale bar: 1 μm.

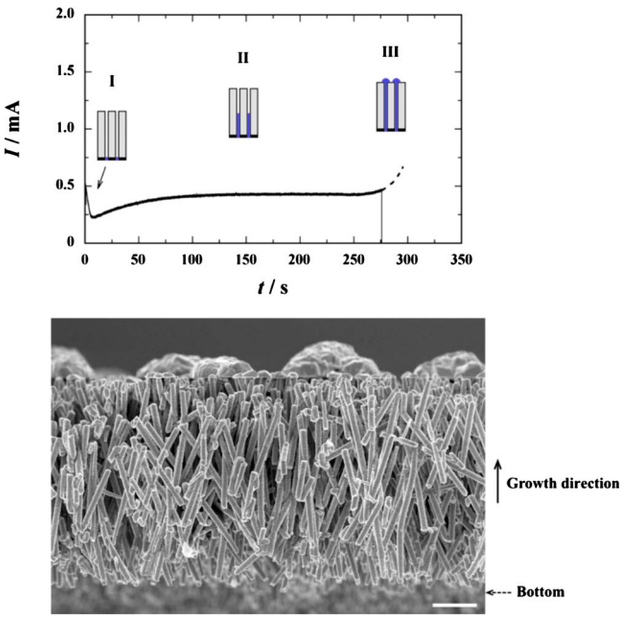

Figure 2. (Color online) Top: Current I vs time t curve for electrodeposition of Cu into the polycarbonate template at $E = -0.4$ V. Cu nanowires grow through the pores and form a capping layer on top of the template. The inset illustrations show the respective growth stages of the nanowires in the template. Bottom: SEM image of Cu nanowire arrays detached from the Pt–Pd cathode layer after the polycarbonate template was removed. The Cu islands on top were created after the nanowires reached the template top surface. Scale bar: 2 μm.

lower than expected in the template, as indicated by the calculations. Therefore, it is understood that Ni nanotube growth is accompanied by H_2 evolution.

Experimental

A polycarbonate-track-etched membrane (Toyo Roshi Kaisha Ltd., Japan) was used as a template for the growth of metal nanostructures. The nominal values of the pore diameter, membrane thickness, and pore density were 200 nm, 10 μm, and 3×10^8 cm^{-2}, respectively. A Pt–Pd alloy layer, with a thickness of roughly 30 nm, was sputtered on one face of the membrane to serve as the cathode. Figure 1 shows a scanning electron microscope (SEM) image of the Pt–Pd surface sputter-deposited on a polycarbonate nanoporous membrane. As can be seen, the pores still show unclosed mouths.[31] The electrochemical cell was found by Motoyama et al.[31,32] and was designed to press the membrane from underneath with a flat Pt sheet to attain good electronic contact with the Pt–Pd cathode and to prevent electrolyte leakage from the bottom. This Pt sheet was connected to a potentiostat.

The electrolyte solutions for Cu and Ni electrodeposition were 0.60 mol L^{-1} $CuSO_4$, 5×10^{-3} mol L^{-1} H_2SO_4, and a mixture of 0.97 mol L^{-1} $NiSO_4$, 0.19 mol L^{-1} $NiCl_2$, and 0.62 mol L^{-1} H_3BO_3.[30] The deposition was conducted under potentiostatic conditions at room temperature. The pH of the Cu plating solution was 1.7. The pH of the Ni solution was regulated down to 3.0, 2.5, 2.0, and 1.5 from the original value of 3.4 by adding sulfuric acid. A 0.5 mm diameter Cu wire of and a 1 mm diameter Ni wire were used as reference electrodes in the respective solutions. The lateral surfaces of these wires were polymer-insulated. Cu and Ni reference electrodes in the above electrolytes showed potentials close to the respective equilibrium potentials of the Cu^{2+}/Cu and Ni^{2+}/Ni couples: +0.33 V (0.60 M $[Cu^{2+}]$) and −0.23 V (1.16 M $[Ni^{2+}]$) vs the standard hydrogen electrode (SHE). In either Cu or Ni deposition, E represents a potential applied with respect to the corresponding reference electrode. Cu and Ni sheets were used as counter electrodes for Cu and Ni electrodeposition, respectively. Metal electrodeposition was conducted within a geometric area of 0.0314 cm^2 of the membrane (2 mm in diameter containing 9.4×10^6 nanopores) defined by a perforated acrylic resin plate.

Current efficiency measurement.— Current efficiency, η (%), is defined as the percentage of the current used for carrying out a desired electrochemical reaction based on Faraday's law.[33] The current efficiency of electrodeposition can be obtained by measuring the weight gain because the side product, H_2 gas,[30,33,34] does not produce any weight gain. In this study, the mass of the deposited metal was analyzed by ICP emission spectrometry. η can be calculated as follows

$$\eta = \int \frac{i_{me}}{i_{me} + i_{H_2}} dt \times 100 = \frac{m/M}{Q/zF} \times 100 \qquad [1]$$

where i_{me} and i_{H_2} are the partial current densities of the metal, either Cu or Ni, and H_2, respectively, m is the mass of deposited metal (g), M is the metal atomic weight (Cu: 63.5 g mol^{-1}; Ni: 58.7 g mol^{-1}), Q is the electrical charge passed (C), z is the valency, and F is Faraday's constant (9.65×10^4 C mol^{-1}).

Figure 2 shows the current transient during Cu deposition into the template at $E = -0.4$ V and an SEM image of electrodeposited Cu nanowire arrays after removing polycarbonate in a dichloromethane solvent. As described in a previous work,[31,32] the current transient curve is classified into four stages: (I) nucleation on the bottom, (II) steady growth in the pores, (III) lateral extension of the metal film on the membrane surface after filling the pores, and (IV) steady growth of a thin film on the membrane (not presented in Fig. 2). The electrolysis was manually stopped immediately after the deposition current began to sharply increase in the beginning of the third stage ($t = 276$ in Fig. 2). This moment corresponded to the growth of nanowires reaching the membrane surface, extending the electrode surface area outside the template, thereby increasing the deposition current. If the circuit was kept closed, the deposition current would have increased, indicated by the broken line. The specimen shown in the SEM image in Fig. 2 was produced by the deposition until the beginning of stage III. Therefore, several Cu islands formed on top.

After electrolysis, the bottom Pt sheet and the template membrane containing the deposited metal were kept separately in dis-

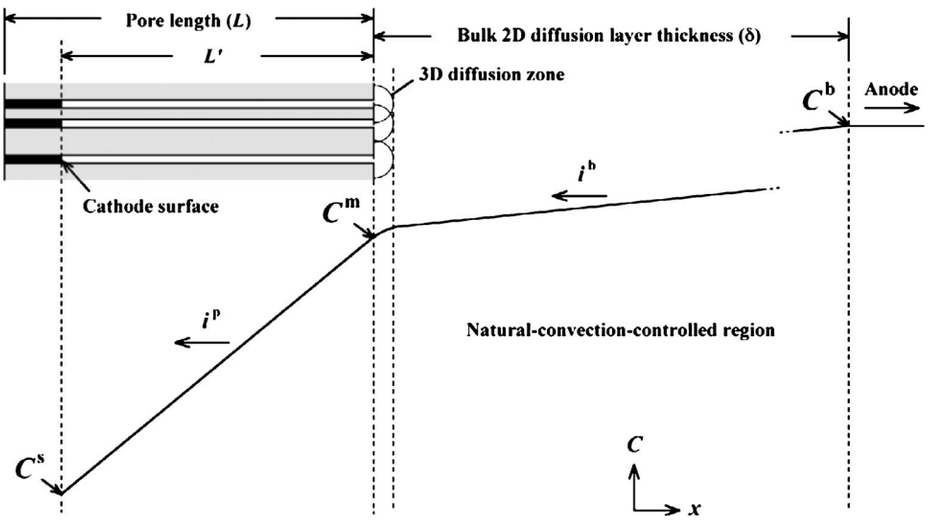

Figure 3. Schematic illustration of the assumed H^+ or Ni^{2+} concentration profile from the cathode surface toward the anode. The hemispherical diffusion zones coalesce each other over the template surface to form the 2D diffusion layer.

tilled water for more than 30 min, and this treatment was repeated. After carefully rinsing with ethanol, the sample and the Pt sheet were dried. Subsequently, they were separately kept in 10 vol % HNO_3 solutions, with a total volume of 50 mL each at 313 K for more than 24 h. A strong HNO_3 solution leached out Cu or Ni embedded in the membrane. The brown or black color, which stemmed from an embedded metal, disappeared within a few hours, giving the region the same appearance as where there was no electrodeposition of the metal. After the solutions cooled down to room temperature, each volume was again adjusted to 50 mL by adding distilled water. Finally, metal concentrations in the HNO_3 solutions were measured by an ICP emission spectrometer (ICAP-575II, Nippon-Jarrel-Ash, Tokyo, Japan). By summing the concentrations of metal ions that leached out of the template and from the Pt sheet, the total mass m in Eq. 1 is calculated.

Surface pH calculation.— This study presumes the following four approximations to simplify the surface pH calculations:

1. All species diffuse through the pores with the same diffusion coefficients and transference numbers as in the bulk solutions.
2. H_2 gas evolution does not affect the ionic mass-transfer rate.
3. Growth of nanowires or nanotubes is negligibly slow compared with the development of a concentration boundary layer outside the template.
4. Natural convection occurs only outside the template.

Regarding the first assumption above, 200 nm diameter seems too large for electric double layers on the template walls to significantly influence the ionic diffusion transports in such concentrated electrolyte solutions (>1 M), according to the literature.[35,36] Although ionic diffusion coefficients in the template pores have to be determined in a reliable way in the future, understanding how the surface concentration differs based only on the geometric difference of the template with fixed diffusion coefficients is significant as a preliminary calculation of this study.

No H_2 bubble was assumed between the cathode surface (nanowire or nanotube ends) and the mouths of the pores. This was because the membrane walls were made hydrophilic [with poly(vinylpyrrolidone)] by the manufacturer, whereby the nucleation of H_2 bubbles in a pore was difficult. The curvature radius of the bubble must be small if it is present in a pore. The bubble inner pressure was considered by the Young–Laplace equation ($p_{in} - p_{out} = 2\gamma/r$, where p_{in} and p_{out} are the inner and outer pressures of a bubble, respectively, and γ is the interfacial energy). For instance, the inner pressure became 14 atm larger than the outer pressure with $\gamma = \sim 0.07$ N m^{-1} [37] and $r = 100$ nm. Hence, H_2 gas molecules were rapidly dissolved into the electrolyte, whereby a bubble was supposed to disappear immediately.[38] The nucleation of a H_2 bubble may possibly occur outside the template if the concentration of the dissolved H_2 gas molecules that diffuses outward from the pores exceeds the critical concentration of the supersaturation. If H_2 gas bubbles form outside the template, they microscopically promote the hydrodynamic velocities of natural convection along the template surface due to buoyancy forces (Appendix A). However, the H_2 partial current per unit geometric area of the template did not exceed 4 mA cm^{-2} in this study. As reported,[39] this range of H_2 partial current density was negligible for the mass-transfer rate. Hence, H_2 gas evolution was not taken into consideration for the ionic mass-transfer rate in this study.

The ionic diffusion layer in a stagnant aqueous electrolyte usually grows 1 order of magnitude greater than 10 μm from vertical electrode surfaces.[40] As the template thickness was 10 μm, the typical time scale for the boundary layer thickness to reach out of the pores was supposed to be $L^2/D \approx 0.1$ s compared to deposition periods of the orders of 10^2 or 10^3 s, which depend on the cathodic potential (L is the pore length and D is the ionic diffusion coefficient). Therefore, the diffusion layer hemispherically developed from all pore openings distributed over the template surface immediately after starting the electrolysis. They coalesced each other, resulting in a planar diffusion layer with a thickness of δ toward the anode.[17,41]

Figure 3 schematically shows the supposed concentration profile of cationic species, i.e., H^+ and Ni^{2+}, from the cathode surface toward the anode located distant enough from the template. The x-axis is defined in the normal direction to the template plane. The distance from the cathode surface to the opening mouths (L') decreases, whereas nanowires or nanotubes grow. i^p and i^b in Fig. 3 are current densities parallel to the x-axis through the pores and across the planar diffusion layer developed outside the template, respectively. C^s is the cathode surface concentration, C^m is the mouth concentration, and C^b is the bulk concentration. A more precise analysis can be addressed with the moving boundary condition applied to the cathode surface to describe a transient diffusion. However, this study measures the current efficiencies averaged over the filling periods. Hence, a precise calculation based on a transient diffusion analysis with a moving boundary does not necessarily meet the concept of the time-averaged current efficiency. In this study, the chemical species concentration at the ends of nanowires or nanotubes is calculated, assuming the steady-state diffusion profile, which would be achieved with a constant length of nanowires or nanotubes.

The cross-sectional fraction of pores in the template can be described by $1 - \exp(-N_p \pi r_p^2)$, where N_p and r_p are the number den-

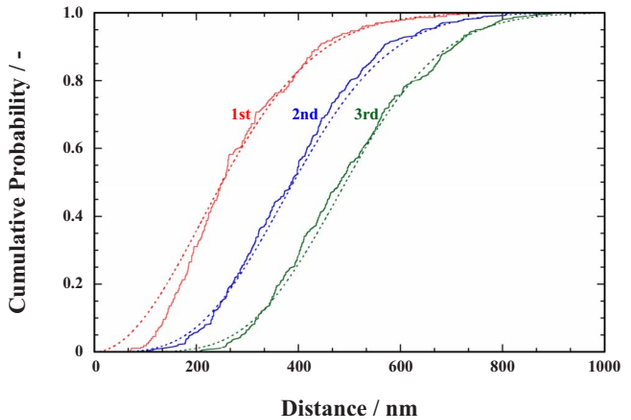

Figure 4. (Color online) Cumulative probabilities for pores to encounter the *n*th (n = 1, 2, 3) nearest neighbors as a function of distance in the 2D arrangements of the template pores. The solid and dotted lines indicate the observed results and the ideal Poisson distribution, respectively.

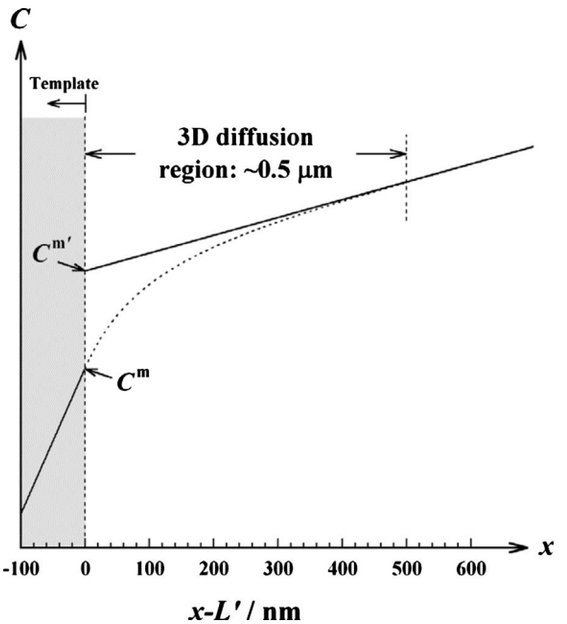

Figure 5. Concentration profile in the vicinity of a mouth. $C^{m'}$ is the intercept at the template surface of the linear 2D diffusion profile. Ionic mass fluxes outside the template converge into the pores through the coalescing 3D diffusion zones. Equation B-2 draws a broken line.

sity of the pores (3×10^8 cm^{-2}) and the pore radius, respectively. Because the pore locations randomly distribute, the Poisson distribution should be applicable.[42-45] Figure 4 shows the respective probabilities to encounter the first, second, and third nearest neighbors. 376 pores in an area of 106 μm^2 were examined by SEM (number density = 3.5×10^8 cm^{-2}). The dotted lines indicate the ideal Poisson distribution expressed by the following equation[45]

$$\frac{dP_n}{dr_n} = \frac{2(\pi N_p)^n r_n^{2n-1}}{\exp(\pi r_n^2 N_p)(n-1)!} \quad [2]$$

where P_n and r_n are the encounter probability and distance to the *n*th nearest neighbors, respectively. Eventually, the Poisson distribution is a good approximation of the template pore arrangement in Fig. 4. The steady-state ionic mass-transfer rates of the inside (i^p/zF) and the outside (i^b/zF) of the template must be balanced as follows

$$i^p = \frac{i^b}{1 - \exp(-N_p \pi r_p^2)} \quad [3]$$

The ionic mass flux across an isoconcentration surface decreases from i^p/zF to i^b/zF, with the distance in the x-direction from the opening mouths to the planar diffusion region. By entirely integrating the ionic mass flux across a plane parallel to the template surface from the template surface ($x = L'$) to the boundary with the bulk concentration region ($x = L' + \delta$), one can obtain the following equation (Appendix B)

$$\frac{C^b - C^{m'}}{\delta} = (C^b - C^m)\left\{\int_0^\delta \frac{dR}{1 - \exp[-N_p \pi (R + r_p)^2]}\right\}^{-1} \quad [4]$$

where $C^{m'}$ is the template surface concentration defined by extrapolating the linear concentration profile in the planar diffusion region to the template surface, and R (cm) is the diffusion field radius from the mouths. The pore diameter actually slightly increases in the middle like a spindle shape, as seen in Fig. 2 and also in the literature.[32,46] Thus, the actual pore volume is increased by a factor of 1.4 based on the shape profile analysis of electron micrographs. Therefore, the r_p value is modified to be 1.18×10^2 nm corresponding to a 1.4-fold volumetric increase from the nominal volume of a pore. Hence, the pore-cross-sectional fraction is 0.12[$=1 - \exp(-N_p \pi r_p^2)$].

Regardless of current density, only the template geometrical characters, N_p and r_p, and the spatial arrangement of pores determine where the hemispherical diffusion fields disappear to shift to a planar field. The deviation of the concentration profile considering the hemispherical diffusion fields from the perfectly linear profile is evident within a distance of ~0.5 μm from the template surface (Fig. 5).

The concentration profile developed from the template surface toward the anode is virtually the same as the one developed from the vertical planar cathode surface toward an anode during electrodeposition with a current density of i^b, except for the microscopic three-dimensional (3D) concentration distribution close to the surface. This is because reactive species are consumed at a constant rate into the pores, as exactly seen on a planar cathode surface having a constant current density. Konishi et al. already demonstrated that natural convection outside the template needs to be taken into consideration.[31] Hence, Eq. 5 is supposed to give a reasonable value of the diffusion layer thickness of δ measured from the template surface as long as the concentration profile near the template surface can be approximated by Fig. 3 [47-49]

$$Sh_y = 0.628 Ra_y^{*1/5} \quad [5]$$

$$Sh_y = \frac{i_{Ni}^b (1 - t^*) y}{zFD_{Ni}\Theta} \quad [6]$$

$$Ra_y^* = \frac{g\alpha i_{Ni}^b (1 - t^*) y^4}{zF\nu D_{Ni}^2} \quad [7]$$

where Sh_y is the Sherwood number, Ra_y^* is the modified Rayleigh number,[49] t^* is the transference number of metal ions, y is the vertical distance from the lower edge of the template (cm), Θ is the difference of $C_{Ni^{2+}}^b$ from $C_{Ni^{2+}}^{m'}$ (mol cm^{-3}), g is the gravitational acceleration (9.8×10^2 cm s^{-2}), α is the densification coefficient for Ni^{2+} ions (cm^3 mol^{-1}), and ν is the kinematic viscosity of the electrolyte (cm^2 s^{-1}). The Sherwood number represents the ratio of convective to diffusive mass-transfer rates. The Rayleigh number represents the ratio of the natural convection mass-transfer rate due to the buoyancy forces to the product of ionic and momentum diffusion coefficients, which means the convective or diffusive mass-transfer rate. Previous work[49] has proved Eq. 5 using vertical planar

Table I. Numerical values of Ni^{2+} ions used for the calculations.[30]

D (cm^2 s^{-1})	6.9×10^{-6}
t^*	0.4
ν (cm^2 s^{-1})	1.5×10^{-2}
α (cm^3 mol^{-1})	1.23×10^{2}

electrodes under low current density conditions. Finally, the diffusion layer thicknesses of Ni^{2+} and H^+ ions measured from the template surface are expressed as

$$\delta_{Ni^{2+}} = \frac{2FD_{Ni^{2+}}\Theta}{i^b_{Ni}} \quad [8]$$

$$\delta_{H^+} = \sigma^* \delta_{Ni^{2+}} \quad [9]$$

where σ^* is the diffusion layer thickness ratio of H^+ ions to Ni^{2+} ions, and σ^* of 1.3 was applied in this study.[39,50,51] As mentioned above, the linear profile is not applicable to the concentration distribution within a range of approximately 0.5 μm from the template surface. However, the calculated diffusion layer thicknesses of δ were always close to 100 μm. Hence, using Eq. 5 is acceptable. Table I summarizes the physical properties of Ni^{2+} ions used for the calculations.

The pH at a given position of x is assumed to be calculated by the local equilibrium of dissociation reactions releasing H^+ and OH^- ions. The water autoprotolysis constant is

$$K_W = C_{H^+}C_{OH^-} = 10^{-14} \ (mol^2 \ L^{-2}) \quad [10]$$

It is assumed that neutral H_2SO_4 molecules are not present in an electrolyte due to perfect dissociation. Both HSO_4^- and SO_4^{2-} are taken into consideration

$$K_{S1} = \frac{C_{SO_4^{2-}}C_{H^+}}{C_{HSO_4^-}} = 10^{-1.92} \ (mol \ L^{-1}) \quad [11]$$

Three dissociation reactions of boric acid ($H_3BO_3 = H_2BO_3 + H^+$, $4H_3BO_3 = HB_4O_7^- + H^+ + 5H_2O$, and $4H_3BO_3 = B_4O_7^{2-} + 2H^+ + 5H_2O$) are also considered.[30,52] Boric acid hardly dissociates in the pH range dealt within this study.[30] To simplify the calculations, the catalytic role of boric ion complexes for Ni deposition, which were pointed out in the literature,[53,54] is not taken into consideration

$$K_{H1} = \frac{C_{H_2BO_3^-}C_{H^+}}{C_{H_3BO_3}} = 10^{-9.21} \ (mol \ L^{-1}) \quad [12]$$

$$K_{H2} = \frac{C_{HB_4O_7^-}C_{H^+}}{(C_{H_3BO_3})^4} = 10^{-6.54} \ (mol^{-2} \ L^2) \quad [13]$$

$$K_{H3} = \frac{C_{B_4O_7^{2-}}(C_{H^+})^2}{(C_{H_3BO_3})^4} = 10^{-15.55} \ (mol^{-1} \ L) \quad [14]$$

We neglect the presence of $NiOH^+$ ions and instead consider $Ni_4(OH)_4^{4+}$ ions $\left[\frac{1}{4}Ni_4(OH_4)^{4+} = Ni^{2+} + OH^-\right]$ [55]

$$K_{N1} = \frac{C_{Ni^{2+}}K_W}{(C_{Ni_4(OH)_4^{4+}})^{1/4}C_{H^+}} = 10^{-7.17} \ (mol^{7/4} \ L^{-7/4}) \quad [15]$$

Finally, 1D steady-state diffusion equations to calculate C^m of H^+ and Ni^{2+} ions can be written as follows[30,56]

$$\frac{i^b_{H_2}}{F} = D_{H^+}\left.\frac{\partial C_{H^+}}{\partial x}\right|_{x=L'} - D_{OH^-}\left.\frac{\partial C_{OH^-}}{\partial x}\right|_{x=L'} + D_{HSO_4^-}\left.\frac{\partial C_{HSO_4^-}}{\partial x}\right|_{x=L'} + nD_{H_3BO_3}\left.\frac{\partial C_{H_3BO_3}}{\partial x}\right|_{x=L'} - 4D_{Ni_4(OH)_4^{4+}}\left.\frac{\partial C_{Ni_4(OH)_4^{4+}}}{\partial x}\right|_{x=L'} \quad [16]$$

$$\frac{i^b_{Ni}(1-t)}{2F} = D_{Ni^{2+}}\left.\frac{\partial C_{Ni^{2+}}}{\partial x}\right|_{x=L'} + 4D_{Ni_4(OH)_4^{4+}}\left.\frac{\partial C_{Ni_4(OH)_4^{4+}}}{\partial x}\right|_{x=L'} \quad [17]$$

where n is

$$n = -\left(\frac{\partial C_{H_2BO_3^-}}{\partial C_{H_3BO_3}} + \frac{\partial C_{HB_4O_7^-}}{\partial C_{H_3BO_3}} + 2\frac{\partial C_{B_4O_7^{2-}}}{\partial C_{H_3BO_3}}\right) \quad [18]$$

Equations 16 and 17 can be rewritten by integration over the concentration boundary layer thickness as follows

$$\frac{i^b_{H_2}}{F}\delta^*_{H^+} = D_{H^+}(C^b_{H^+} - C^m_{H^+}) - D_{OH^-}K_W\frac{C^b_{H^+} - C^m_{H^+}}{C^b_{H^+}C^m_{H^+}} + D_{HSO_4^-}(C^b_{HSO_4^-} - C^m_{HSO_4^-}) + D_{H_3BO_3}(C^b_{H_2BO_3^-} - C^m_{H_2BO_3^-}) + D_{H_3BO_3}(C^b_{HB_4O_7^-} - C^m_{HB_4O_7^-})$$
$$+ 2D_{H_3BO_3}(C^b_{B_4O_7^{2-}} - C^m_{B_4O_7^{2-}}) - 4D_{Ni_4(OH)_4^{4+}}(C^b_{Ni_4(OH)_4^{4+}} - C^m_{Ni_4(OH)_4^{4+}}) \quad [19]$$

$$\frac{i^b_{Ni}(1-t)}{2F}\delta^*_{Ni^{2+}} = D_{Ni^{2+}}(C^b_{Ni^{2+}} - C^m_{Ni^{2+}}) + 4D_{Ni_4(OH)_4^{4+}}(C^b_{Ni_4(OH)_4^{4+}} - C^m_{Ni_4(OH)_4^{4+}}) \quad [20]$$

where we define δ^* as

$$\delta^* = \int_0^{\delta}\frac{dR}{1 - \exp[-N_p\pi(R + r_p)^2]} \quad [21]$$

where δ^* represents the total diffusion path length, taking the nonlinear diffusion in close vicinity of the template surface into consideration (see Eq. 4). The optimum C^m values obtained from Eq. 19 and 20 were then substituted as the boundary conditions into the following equations, which describe the diffusions through the pores

$$\frac{i^{p}_{H_2}}{F} = D_{H^+}\left.\frac{\partial C_{H^+}}{\partial x}\right|_{x=0} - D_{OH^-}\left.\frac{\partial C_{OH^-}}{\partial x}\right|_{x=0} + D_{HSO_4^-}\left.\frac{\partial C_{HSO_4^-}}{\partial x}\right|_{x=0} + nD_{H_3BO_3}\left.\frac{\partial C_{H_3BO_3}}{\partial x}\right|_{x=0} - 4D_{Ni_4(OH)_4^{4+}}\left.\frac{\partial C_{Ni_4(OH)_4^{4+}}}{\partial x}\right|_{x=0} \quad [22]$$

$$\frac{i^{p}_{Ni}}{2F} = D_{Ni^{2+}}\left.\frac{\partial C_{Ni^{2+}}}{\partial x}\right|_{x=0} + 4D_{Ni_4(OH)_4^{4+}}\left.\frac{\partial C_{Ni_4(OH)_4^{4+}}}{\partial x}\right|_{x=0} \quad [23]$$

Likewise, Eq. 22 and 23 are rewritten as

$$\frac{i^{p}_{H_2}}{F}L' = D_{H^+}(C^{m}_{H^+} - C^{s}_{H^+}) - D_{OH^-}K_W\frac{C^{m}_{H^+} - C^{s}_{H^+}}{C^{m}_{H^+}C^{s}_{H^+}} + D_{HSO_4^-}(C^{m}_{HSO_4^-} - C^{s}_{HSO_4^-}) + D_{H_3BO_3}(C^{m}_{H_2BO_3^-} - C^{s}_{H_2BO_3^-}) + D_{H_3BO_3}(C^{m}_{HB_4O_7^-} - C^{s}_{HB_4O_7^-})$$
$$+ 2D_{H_3BO_3}(C^{m}_{B_4O_7^{2-}} - C^{s}_{B_4O_7^{2-}}) - 4D_{Ni_4(OH)_4^{4+}}(C^{m}_{Ni_4(OH)_4^{4+}} - C^{s}_{Ni_4(OH)_4^{4+}}) \quad [24]$$

$$\frac{i^{p}_{Ni}(1-t)}{2F}L' = D_{Ni^{2+}}(C^{m}_{Ni^{2+}} - C^{s}_{Ni^{2+}}) + 4D_{Ni_4(OH)_4^{4+}}(C^{m}_{Ni_4(OH)_4^{4+}} - C^{s}_{Ni_4(OH)_4^{4+}}) \quad [25]$$

The total numbers of sulfur and boron atoms were kept invariable at $x = 0$, L', and δ_{H^+}

$$C_{HSO_4^-} + C_{SO_4^{2-}} = C_S \ (\text{mol L}^{-1}) \quad [26]$$

$$C_{H_3BO_3} + C_{H_2BO_3^-} + 4C_{HB_4O_7^-} + 4C_{B_4O_7^{2-}} = 0.62 \ (\text{mol L}^{-1}) \quad [27]$$

C_S are 2×10^{-2}, 5×10^{-3}, 1×10^{-3}, 3×10^{-4}, and 0 at pH 1.5, 2.0, 2.5, 3.0, and 3.4, respectively. The following mass balance equation for Ni atoms was also considered at $x = \delta_{Ni^{2+}}$

$$C^{b}_{Ni^{2+}} + 4C^{b}_{Ni_4(OH)_4^{4+}} = 1.16 \ (\text{mol L}^{-1}) \quad [28]$$

Table II shows the diffusion coefficients of the chemical species. The optimum $C^{s}_{H^+}$ value of Eq. 24 and 25 gives the pH value at the cathode surface in the template.

Results and Discussion

Measurement method evaluation.— The Cu^{2+}/Cu couple has a more positive equilibrium potential ($E^0 = +0.33$ V vs SHE, 0.60 M $[Cu^{2+}]$) than the hydrogen couple (H^+/H_2). Hence, near 100% current efficiency of Cu deposition can be expected.[59,60] Before the Ni current efficiency measurements, we examined whether the Cu current efficiency obtained by the present procedure reached 100% or not to ensure the subsequent discussion of Ni current efficiency.

Two potentials, $E = -0.25$ and -0.40 V, were tested. When E was lowered from -0.25 to -0.40 V, the deposition current increased by a factor slightly greater than 2, and the filling period was shortened by half. Figure 6a and b shows the mass frequency distributions of Cu nanowires electrodeposited at $E = -0.25$ and -0.40 V, respectively. Ten samples were analyzed at each potential. The mean values (μ) of 40 μg ($E = -0.25$ V) and 41 μg ($E = -0.40$ V) were almost the same. The standard deviations (σ) were 3.7 and 8.9 μg, respectively. The detected mass of Cu deposited on the bottom Pt sheet was always less than 5% ($< \sim 2$ μg) of the mass detected from the template. This mass value was less than the

Table II. Diffusion coefficients used for the calculations.

Species	Diffusion coefficient ($cm^2\ s^{-1}$)	Reference
H^+	5.0×10^{-5}	57
OH^-	1.0×10^{-5}	57
HSO_4^-	1.1×10^{-5}	56
H_3BO_3	1.1×10^{-5}	58
$Ni_4(OH)_4^{4+}$	4.3×10^{-6}	55

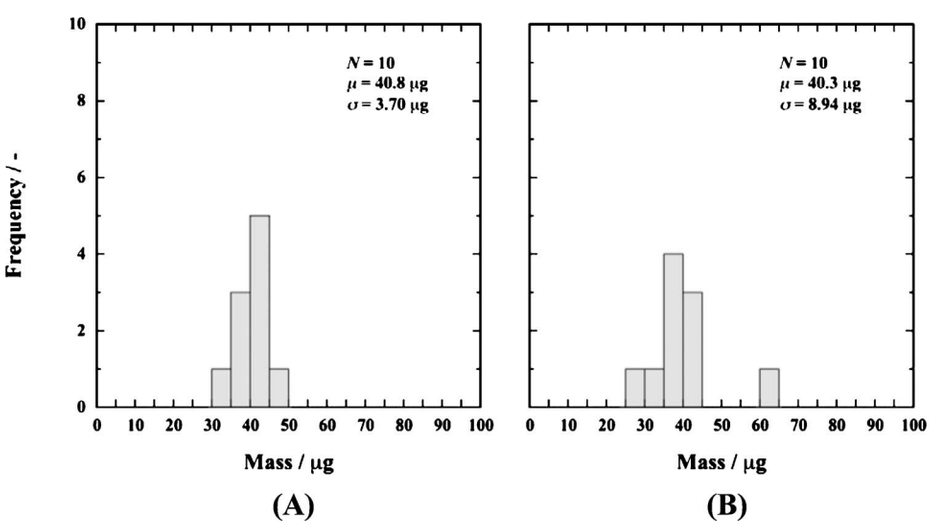

Figure 6. *m* frequency distributions of Cu deposited at (a) $E = -0.25$ V and (b) $E = -0.4$ V (N: sample number; μ: mean; σ: standard deviation).

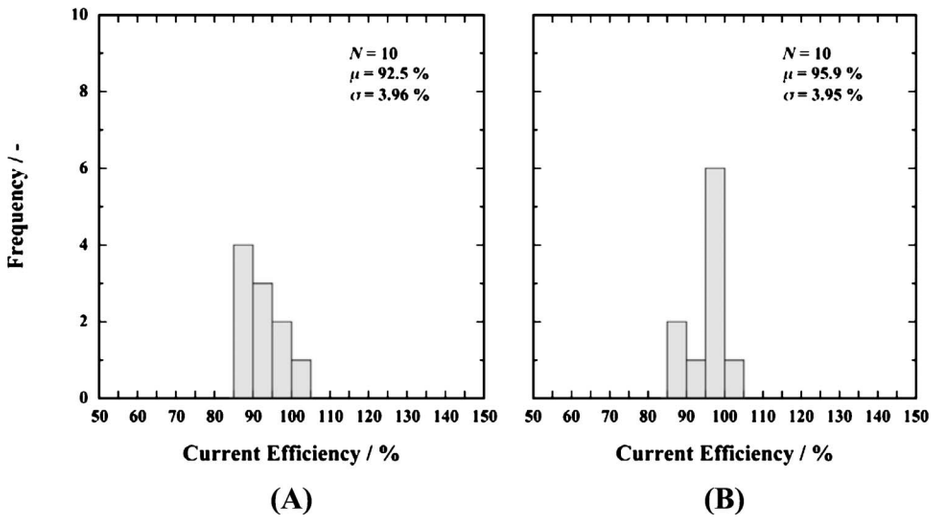

Figure 7. η frequency distributions obtained from the Cu deposition at (a) $E = -0.25$ V and (b) $E = -0.4$ V (N: sample number; μ: mean; σ: standard deviation).

standard deviation. Therefore, the extra Cu deposition on the bottom Pt sheet did not damage the concept of measuring current efficiency achieved by Cu deposition into the porous template.

The nominal values of the pore diameter and pore density are 200 nm and 3×10^8 cm^{-2}, respectively. Hence, the mass of Cu completely filling in the pores of the template with a geometric area of 0.0314 cm^2 is 27 μg, with a bulk Cu density of 8.96 g cm^{-3}. As mentioned above, the actual pore volume is approximately 1.4 times larger than the perfect columnar shape having a nominal diameter of 200 nm. As a result, $27 \times 1.4 = 38$ μg agrees with the above mean values of the measured data. This agreement supports the soundness of the present measurement technique for current efficiency.

Figure 7a and b shows the distributions of the measured current efficiency, η. It ranged from 88.2 to 100% at $E = -0.25$ V and from 89.9 to 102% at $E = -0.40$ V. The average efficiencies were 92.5% ($E = -0.25$ V) and 95.9% ($E = -0.40$ V) with almost the same standard deviations of 4.0%. The measured efficiencies were slightly lower than 100%. The reason that the Cu deposition had a current efficiency less than 100% needs further investigation. However, the positive facts of η near 100% and a narrow distribution (4.0% standard deviation) encouraged us to measure Ni current efficiency with the present technique. We postulate that the Ni current efficiency, presented below, is sufficiently reliable.

Calculated pH value in template.— Figure 8 shows variations in the cathode surface pH (pH^s) in a porous template as a function of H_2 partial current density, calculated with various bulk pH values (pH^b). The calculation parameters were $N_p\pi r_p^2 = 0.1$, $L' = 1$ μm, and $i_{Ni}^p = 10$ mA cm^{-2}. A dotted line indicates the pH values at the opening mouths (pH^m) for each pH^b value. In any case, the cathode surface pH value suddenly shows a steep increase from the bulk value to more than 6 at a particular current density. This is the typical behavior of a cathode surface pH as a function of H_2 partial current density.[30,56] Because L' is only 1 μm, the cathode surface is not distant from the mouths. Hence, pH^s is always close to pH^m, except for the current density region where it increases steeply. As pH^b becomes higher, smaller H_2 partial current densities cause a steep increase in pH^s. However, H_2 partial current densities greater than 10–30 mA cm^{-2} are impractical for Ni electrodeposition. Additionally, the third assumption listed above also becomes unreasonable. Hence, practically, pH^s hardly increases when pH^b is 1.5 or 2, as shown in Fig. 8. The decrease in the Ni^{2+} concentration at the cathode surface in the template from the bulk concentration was ~3% of the bulk in the calculations of this figure.

Figure 9 shows the variations in pH^s with pH^b 1.5 as a function of H_2 partial current density with various distances from the cathode surface to the mouths (L'). The pH^5 values of a vertical planar cathode are also shown. The concentration gradient near the template surface ($\partial C/\partial x$ at $L' \le x \le L' + \delta$) is one-tenth of that for a vertical planar cathode because $1 - \exp(-N_p\pi r_p^2)$ is equal to 0.1 (see the inset of Fig. 9). The diffusion layer thicknesses are not so different as the concentration gradients are because of Eq. 5-8 ($\delta \propto i^{-1/5}$). Consequently, pH^m is maintained much lower than pH^s of a vertical planar cathode with the same H_2 partial current density at the cathode. As L' increases, pH^s in the template increases while approaching a vertical planar cathode because the diffusion path from the opening mouths to the cathode surface becomes longer. If L' becomes greater than the diffusion layer thickness of a vertical planar cathode (> ~ 100 μm), pH^s in the template becomes higher than pH^s of a vertical planar cathode in the calculation.

Figure 10 shows the variations in pH^s with pH^b 1.5 as a function of H_2 partial current density with various pore-cross-sectional-fraction values, $1 - \exp(-N_p\pi r_p^2)$. With the same H_2 partial current density at the cathode, a larger proton flux is needed toward the

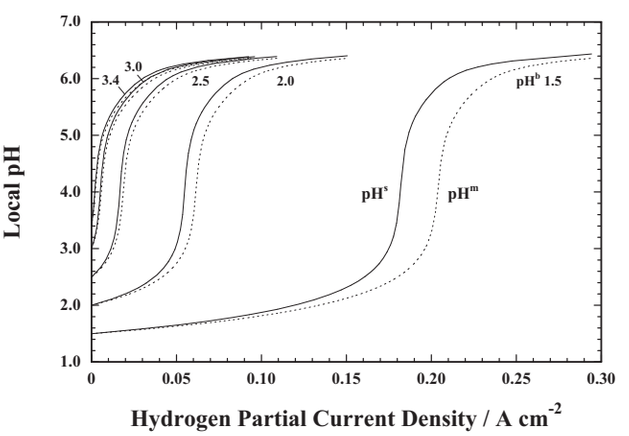

Figure 8. Local pH variations with different bulk solution pH values (pH^b 1.5, 2.0, 2.5, 3.0, and 3.4) as a function of H_2 partial current density. pH^b corresponds to pH values at a H_2 partial current density of zero. The dotted and solid lines indicate pH values at the mouths (pH^m) and the cathode surface (pH^s), respectively. The calculation parameters for this figure are $N_p\pi r_p^2 = 0.1$, $L' = 1$ μm, and $i_{Ni}^p = 10$ mA cm^{-2}.

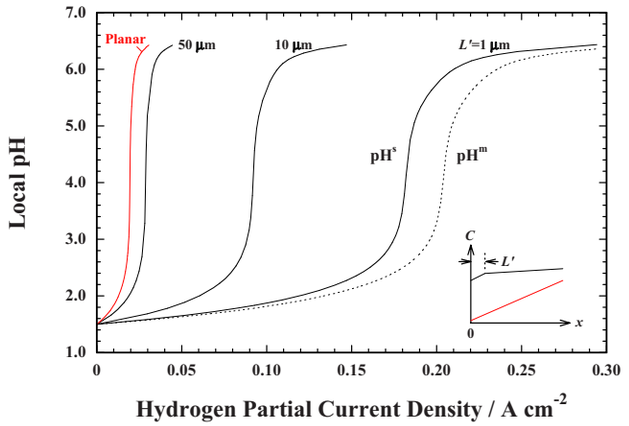

Figure 9. (Color online) Local pH variations with different L' values as a function of H_2 partial current density. The dotted line indicates pH^m. The solid lines indicate pH^s for nanoporous templates and a vertical planar cathode. The calculation parameters for this figure are $N_p\pi r_p^2 = 0.1$, pH^b 1.5, and $i_{Ni}^p = 10$ mA cm^{-2}. The inset figure shows the concentration profiles for the porous-template deposition (higher concentration profile) and planar-cathode deposition (lower concentration profile) with the same current density at the cathode surfaces ($x = 0$).

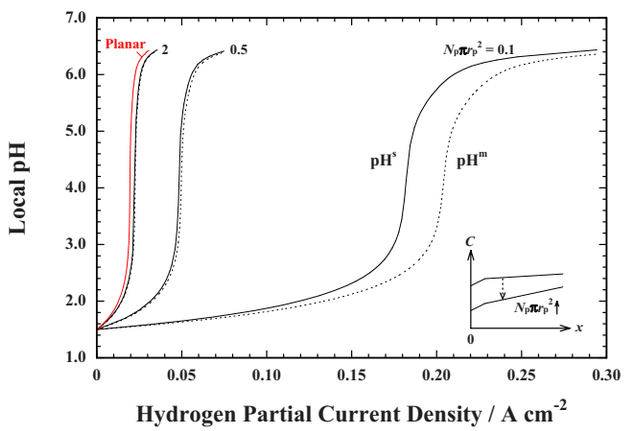

Figure 10. (Color online) Local pH variations with different $N_p\pi r_p^2$ values as a function of H_2 partial current density. The dotted line indicates pH^m. The solid lines indicate pH^s for nanoporous templates and a vertical planar cathode. The calculation parameters for this figure are $L' = 1$ μm, pH^b 1.5, and $i_{Ni}^p = 10$ mA cm^{-2}. The pore-cross-sectional fractions with $N_p\pi r_p^2 = 0.1$, 0.5, and 2 correspond to 0.095, 0.39, and 0.86, respectively. The inset figure shows two different concentration profiles for the porous-template deposition with the same current density at the cathode surfaces ($x = 0$). The top profile has a smaller $N_p\pi r_p^2$ value than the lower profile.

Table III. Summary of Ni nanostructures deposited at various potentials and pH. Meanings of the superscripts (A) and (B) are explained in the text.

E (V)	pH	Structure	Tube wall thickness (nm)
−0.7	1.5	Tube/wire	20–30
−0.7 (B)	3.4	Tube/wire	20–50
−0.7	5.5	Tube/wire	50–70
−0.8 (B)	3.4	Wire	—
−0.9 (B)	3.4	Wire	—
−1.0 (A)	1.5	Tube/wire	10
−1.0 (A)	2.0	Tube/wire	20–30
−1.0 (A)	2.5	Wire	—
−1.0 (A)	3.0	Wire	—
−1.0 (A),(B)	3.4	Wire	—
−1.0	5.5	Wire	—

template with a greater pore-cross-sectional fraction (see the inset of Fig. 10). With the same $i_{H_2}^p$, $i_{H_2}^b$ becomes greater with increasing $N_p\pi r_p^2$ (Eq. 3). The pH^m and pH^s values approach a vertical planar cathode, as $1 - \exp(-N_p\pi r_p^2)$ increases toward 1.

In summary, the pH at the cathode surface in the template is lower when compared to a vertical planar cathode unless L' is longer than the diffusion layer thickness for a vertical planar cathode. Additionally, the smaller the pore-cross-sectional fraction, the harder it is for the cathode surface pH to increase.

Ni nanostructure morphologies.— The morphologies of the electrodeposited Ni nanostructures were examined for several conditions. As shown in Fig. 11a, Ni began to grow and form hollow tube structures because the template had unclosed mouths at the bottom[61] (see Fig. 1). Subsequently, Ni grew toward the core and quickly formed solid wires leaving the initial hollow structure behind (Fig. 11b).

However, as the solution pH value was sequentially decreased from 3.4 to 3.0, 2.5, 2.0, and 1.5 with a constant potential of −1.0 V, some of the nanostructures began to show entirely uniform hollow nanotubes. Moreover, the cathode potential was also critical. As the cathode potential became more positive with constant pH 3.4 or 5.5, some nanotubes grew longer at $E = -0.7$ V. The results of the transmission electron microscope (TEM) observations are summarized in Fig. 11c-i and Table III. The tube walls became as thin as 10 nm at $E = -1.0$ V and pH 1.5 (Fig. 11e), whereas they increased to 70 nm at $E = -0.7$ V and pH 5.5 (Fig. 11d and h). Grain morphologies were also different depending on the tube wall thickness. Grain sizes became greater up to 30–50 nm at $E = -0.7$ V and pH 3.4 (Fig. 11g), but the tube walls with 50–70 nm in thickness deposited at pH 5.5 did not show large grains (Fig. 11d and h). The tube walls were conformally deposited on the template walls (Fig. 11f). TEM exhibits the presence of the hollow interiors by clear contrast with the tube walls, and hence nanowires appear to be dark totally (Fig.

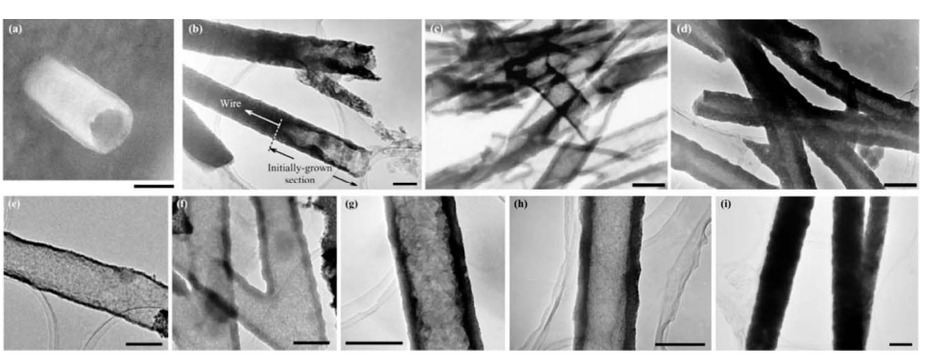

Figure 11. (a) SEM image of an initially grown Ni hollow structure on the Pt–Pd cathode. The template was removed by dichloromethane solution ($E = -1.0$ V, pH 3.4). [(b)-(i)] TEM images of various Ni nanostructures. (b) Nanowires with hollow sections introduced in the initial stage of the deposition ($E = -1.0$ V, pH 3.4). [(c) and (g)] Nanotubes deposited at $E = -0.7$ V, pH 3.4; [(d) and (h)] $E = -0.7$ V, pH 5.5; (e) $E = -1.0$ V, pH 1.5; and (f) $E = -1.0$ V, pH 2.0. (i) Nanowires deposited at $E = -1.0$ V, pH 3.0. All scale bars: 200 nm.

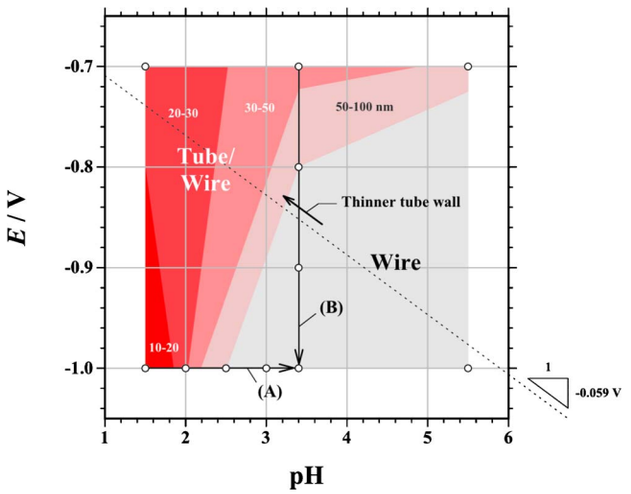

Figure 12. (Color online) *E*–pH diagram with contours of the nanotube wall thickness. Values in each shaded domain indicate the corresponding range of tube wall thicknesses. The potential *E* is measured with respect to a Ni reference electrode used. The arrows of (A) and (B) in the diagram indicate directions where tube-to-wire transitions occur with a constant potential of −1.0 V and a constant pH of 3.4, respectively. The dotted line with a slope of −0.059 V (pH unit)$^{-1}$ is parallel to the H^+/H_2 equilibrium potential line.

11i). The tube-to-wire transition identified along with (A), the pH variation from 1.5 to 3.4 at a constant potential of −1.0 V, and (B), the potential variation from −0.7 to −1.0 V at constant pH 3.4 is focused on in this work.

Figure 12 shows the distribution of the nanotube wall thickness as a function of pH and potential. Blank circles indicate conditions where experiments and morphological observations were conducted, as listed in Table III. The wall thickness variations between plots were linearly interpolated, and the positions having the same values were connected with straight contour lines. A nanotube wall thickness of 100 nm was assigned to the region where only nanowires were deposited. Extensive experiments on Ni electrodeposition made it possible to draw the interpolation or contour lines corresponding to the various nanotube wall thicknesses in the diagram. Figure 12 indicates that a transition from the nanotube to the nanowire occurs in the direction toward the more acidic or less noble corner. The domain for the nanotube deposition is definable as a function of the pH and potential. The H^+/H_2 equilibrium potential line [slope: −0.059 V (pH unit)$^{-1}$] roughly forms a right angle with the contours in this figure. This may suggest that nanotube walls become thinner when the overpotential for Ni deposition decreases, whereas that for H_2 evolution remains constant. The nanotube walls gradually become thicker through transition path (A), whereas transition (B) shows a sudden increase from −0.7 to −0.8 V.

Measured current efficiency.— In the above calculations, the pH at the cathode surface in the template is lower than that at the vertical planar cathode surface. Hence, the current efficiency is expected to be lower when carrying out Ni electrodeposition in the nanoporous template compared to a vertical planar cathode. Figure 13 shows measured current efficiencies η as functions (A) of the pH at a constant potential of −1.0 V and (B) of the potential at constant pH 3.4. Three samples were analyzed for each condition. The results show that η is approximately 75% at pH 1.5 ($E = -1.0$ V) and increases with pH, resulting in almost 100% at pH greater than 2.0 (Fig. 13A). In Fig. 13B, the measured efficiency shows approximately 85% at $E = -0.7$ V and linearly increases to almost 100% at $E = -1.0$ V.

Current efficiencies obtained with a vertical planar cathode (size: 1 × 1 cm) are also expressed with cross marks as reference values.[30] Current efficiency during the nanotube deposition at pH 1.5 ($E = -1.0$ V) is lower than that of a vertical planar cathode in Fig. 13A. Figure 13B also indicates that current efficiency at $E = -0.7$ V, where nanotubes are deposited, is much lower compared to a vertical planar cathode. Hence, Fig. 13A and B suggests that the nanotube deposition starts to occur as the ratio of the Ni deposition rate to the H_2 evolution rate decreases.

Additionally, the current efficiency is measured at $E = -0.7$ V and pH 1.5. The average current efficiency is as low as 25% (Fig. 13C), and it has a large standard deviation, suggesting significant fluctuations in the balance between Ni deposition and H_2 gas evolution. Nanotubes with 20 nm thick walls were deposited under this condition (see Table III).

Fukunaka et al. discussed the possible physical model of nanotube growth.[15] The membrane walls are so hydrophilic that if nucleated, a H_2 bubble prefers to have contact areas with the inner walls of a Ni nanotube. The inner pressure of a 100 nm diameter bubble is 10–20 atm higher than the outer pressure.[38] When the H_2 evolution rate is continuously balanced with the dissolution rate at the front face of a H_2 bubble trapped in the center at the end of a nanotube, the bubble does not disappear and maintains the hollow core during the deposition. Dissolved H_2 gas molecules diffuse outward from the pores, and macroscopic gas bubbles start to nucleate outside the pores if the dissolved H_2 concentration out of the membrane exceeds the critical concentration of the supersaturation. However, there are still questions that need investigation. For instance, why are bubble sizes uniform in every pore where a nanotube grows? What is the effect of nickel hydride on nanotube growth? How does the interfacial energy between Ni and polycarbonate play a role in the deposition process? The present study does not answer these questions but quantitatively shows that the current efficiency drops when nanotubes are electrodeposited as compared to nanowires.

Calculated cathode surface pH.— Partial current density of Ni in the template can be written as follows

$$i_{Ni}^{p} = \frac{zF\rho L}{Mt_{P}} \qquad [29]$$

where ρ is the mass density of Ni (8.90 g cm^{-3}) and t_p is a filling period (s) from $t = 0$ until the time when the deposition current starts to sharply increase, as presented in Fig. 2. This equation calculates i_{Ni}^{p} independently of the pore diameter, which deviates from the nominal value of 200 nm. The membrane thickness is, however, quite close to 10 μm (see Fig. 2). Transient information is lost when using Eq. 29, but the current efficiencies measured in this work are averaged over the filling periods. Hence, it is reasonable to estimate the partial current density of Ni based on Eq. 29 rather than a recorded current divided by the total pore cross-sectional area based on the nominal values. The H_2 partial current density, $i_{H_2}^{p}$, is given by $i_{Ni}^{p}(100/\eta - 1)$.

Figure 14A and B shows partial current densities of Ni and H_2. The Ni partial current density increases from 75 to more than 100 mA cm^{-2} by increasing the pH (Fig. 14A). However, the H_2 partial current density decreases with pH. The $i_{H_2}^{p}$ shows as large as 30 mA cm^{-2} at pH 1.5 where nanotubes with the thinnest walls are deposited. As the H_2 partial current density increases, the Ni deposition rate becomes smaller even at the same potential of −1.0 V.

The Ni partial current density increases as the potential becomes more negative (Fig. 14B), but the results from the vertical planar cathode are much larger than expected, especially at $E = -0.7$ and −0.8 V. The H_2 partial current density also tends to increase as the potential becomes more negative toward −1.0 V. Hence, the Ni deposition rate is smaller when nanotubes are deposited compared to a vertical planar cathode. The slope of the Ni partial current density, with respect to the potential, is clearly steeper than that of the H_2 partial current density.

Figure 15 shows the local pH values in the templates during the Ni electrodeposition, calculated with $L' = 5$ μm, assuming the cathode surface is in the middle of the pores. When the bulk solution

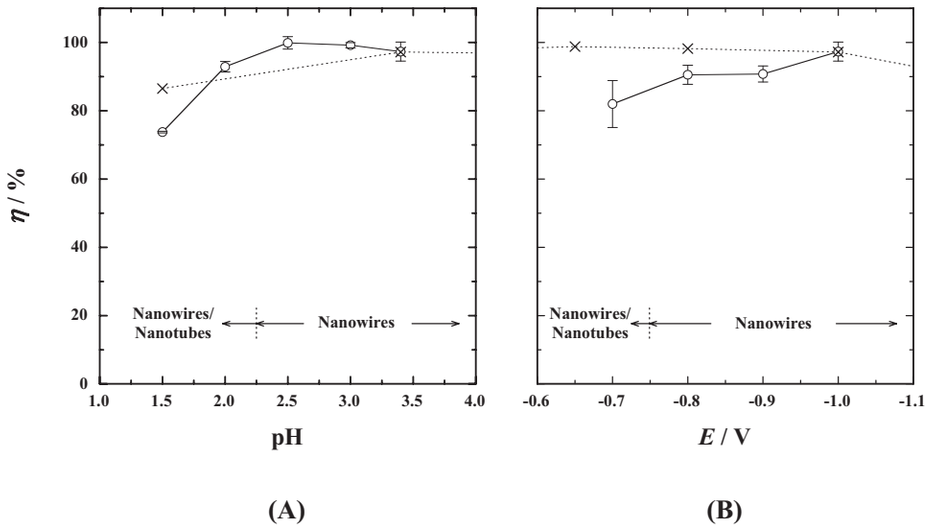

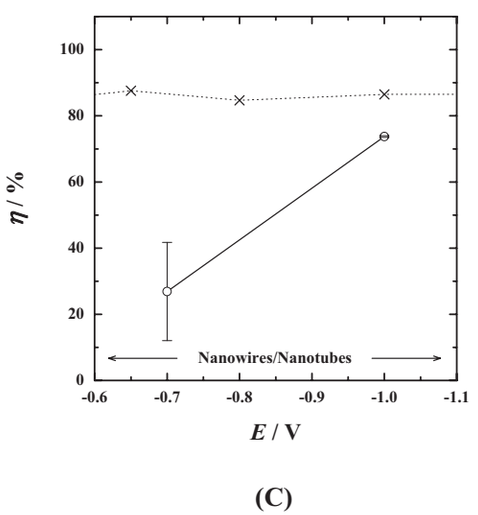

Figure 13. Variations in Ni current efficiencies as functions of (A) pH at a constant potential of −1.0 V, (B) potential at a constant pH of 3.4, and (C) potential at a constant pH of 1.5. (–○–) nanoporous template and (--×--) vertical planar cathode.[30]

pH is smaller than 3.0 ($pH^b \leq 3.0$), the pH values at the mouths and the cathode surface hardly increase from pH^b (Fig. 15A). pH^s finally rose to approximately 5 at pH^b 3.4. Figure 15B also shows that the pH^s values in the templates were 1 to 2 lower when compared to a vertical planar cathode. At $E = -0.7$ V and pH 1.5 (plot not shown), the pH^s in the template was almost 1.5 compared to 2–3 for a vertical planar cathode. These results may explain why H_2 evolution occurs more significantly in the template than on a vertical planar cathode as shown in Fig. 13. Moreover, pH^s tended to be lower when the nanotubes were deposited in tube-to-wire transition paths (A) and (B).

Figure 16 shows an *E*–pH diagram reorganized with the calculated pH^s values. The respective distributions of the measured current efficiency and tube wall thickness, which are linearly interpolated, are superimposed in the diagram. As already discussed in Fig. 12, tracing a line parallel to the H^+/H_2 equilibrium potential in the positive direction means that the overpotential for Ni electrodeposition decreases while keeping that for H_2 evolution constant. Hence, it is comprehensible that the η monotonically decreases toward the more acidic and noble corner along the dotted line in Fig. 16. The tube wall thickness distribution in Fig. 16 is not significantly different from Fig. 12 because pH^s hardly increases from the original bulk values except for that at pH^b 3.4. Therefore, the trend, observed in Fig. 12, that the tube wall thickness decreases as the dotted line is traced in the positive direction is still observed in Fig. 16. When the η and tube wall thickness distributions are compared, the directions for them to decrease are roughly consistent in the diagram. This result clearly shows that H_2 evolutions promote nanotube growth. However, the tube wall thickness variation does not follow the η contours toward the more acidic and less noble corner where the thinnest wall tubes were observed. This may indicate the complexity in the deposition process of the nanotubes. The absolute H_2 evolution rate seems also critical for the nanotubes to determine the tube wall thickness.

We showed a clear correlation between the nanotube deposition and H_2 evolution. As predicted by the calculations, the measured current efficiency in the nanoporous template was lower than a vertical planar cathode. We observed an interesting trend that nanotubes with thinner walls were electrodeposited as the current efficiency decreased. The Ni deposition rate was slightly smaller when nanotubes grew compared to nanowires. From the calculated results, the pH values in the template were more than 1 to 2 times smaller than at the vertical planar cathode surface. The assumptions used for the calculation need to be more severely examined in the future. We emphasize that the reactive species concentrations at the cathode surface in the template tend to be higher than that of a macroscopic

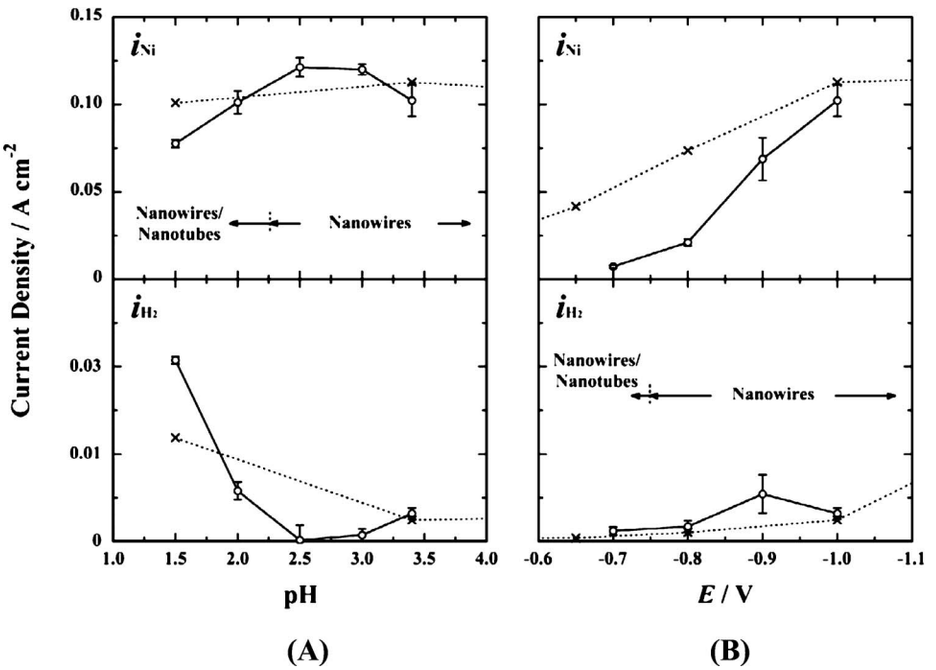

Figure 14. Ni and H_2 partial current densities as functions of (A) pH at a constant potential of −1.0 V and (B) potential at a constant pH of 3.4. (–○–) nanoporous template and (--×--) vertical planar cathode.[30]

planar cathode. This understanding is suspected to also be important in the electrodeposition of Ni–Fe nanowires.[56,62,63]

Conclusions

We have investigated H_2 evolution rates at the cathode surface during Ni electrodeposition in polycarbonate membrane templates with pore diameters of 200 nm under various pH and potential conditions. The calculation model of the pH value at the cathode surface in the template was presented. The calculations revealed that the cathode surface pH was lower in the template than at the vertical planar cathode surface. TEM observed the morphologies of Ni nanostructures deposited into the template. Nanotubes with thinner walls were deposited under more acidic and less noble conditions. ICP spectrometry also allowed the determination of the current efficiency of Ni electrodeposition. The calculations indicated that the pH was lower at the cathode surface in the template than at the vertical planar cathode surface. The measured current efficiency was lower in the template compared to a previous work that employed a

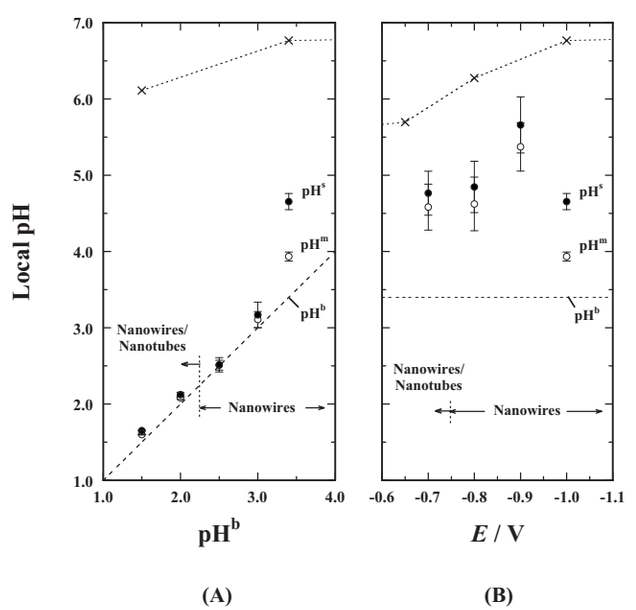

Figure 15. The calculated local pH values as functions of (A) pH at a constant potential of −1.0 V and (B) potential at a constant pH of 3.4. (●) pH^s: pH at the cathode surface, which is assumed to be 5 μm recessed from the mouths in these calculations; (○) pH^m: pH at the mouths; and (--×--) vertical planar cathode.[30] The pH^b indicates the bulk pH with a broken line.

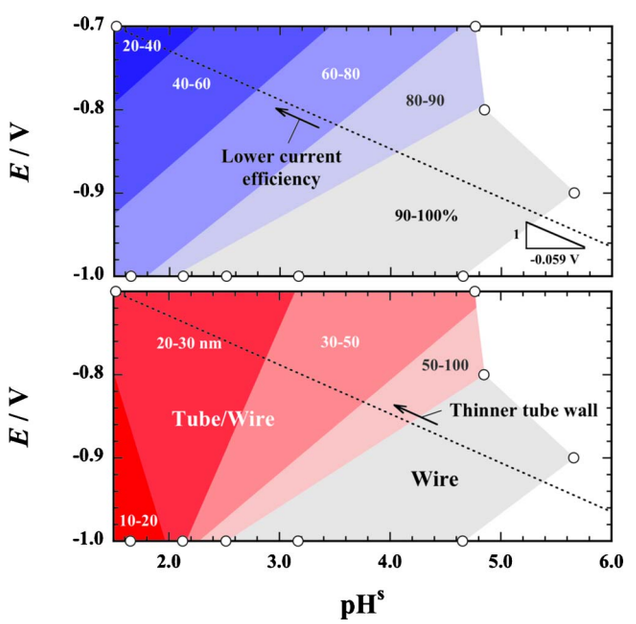

Figure 16. (Color online) Contours of (top) the measured current efficiency and (bottom) observed tube wall thickness in the E–pH^s diagram. The potential E is measured with respect to a Ni reference electrode used. Values in each shaded domain indicate the corresponding range of current efficiency or tube wall thickness. The dotted lines are the same line with a slope of −0.059 V (pH unit)$^{-1}$. Only the region where the cathode surface pH was calculated is shaded.

vertical planar cathode, as expected by the calculations. Moreover, the current efficiency tended to be lower when nanotubes with thinner walls were electrodeposited. Therefore, we concluded that significant H_2 evolution sustained electrochemical growth of Ni nanotubes in the template.

Acknowledgment

Part of this work was supported by the 21st Century Center of Excellence (COE) Program and the Ministry of Education, Science and Culture (grant-in-aid for Exploration Research no. 15360402). We thank Professor R. Hagiwara, Professor T. Sakka, Professor S. Kikuchi, and Professor K. Sumiyama for helpful discussions and Professor T. Kuzuya for assistance with the TEM observations and M. Hamura for assistance with the ICP measurements.

Waseda University assisted in meeting the publication costs of this article.

Appendix A

When H_2 gas evolution rate significantly enhances the ionic mass-transfer rate, the contribution of micromixing caused by evolving gas bubbles on the cathode surface has to be taken into account, in addition to macromixing based on the Rayleigh number modified by the density difference of gas/electrolyte dispersion layers accompanying upward natural convection.[39]

Appendix B

In close vicinity of the template surface, a diffusion field hemispherically develops from every mouth. An isoconcentration surface can be defined by the outer surface of those coalescing domes with the same radii of R. Ionic mass flux lines are kept normal to the isoconcentration surface and converged into the pores from the two-dimensional (2D) diffusion region outside the template. By considering the projected area of a nonplanar isoconcentration surface, an ionic mass flux at a giving position is approximated as[43]

$$i_{(R)} = \frac{i^{\mathrm{b}}}{1 - \exp[-N_{\mathrm{p}}\pi(R + r_{\mathrm{p}})^2]} \qquad \text{[B-1]}$$

where $i_{(R)}$ is a current density at a distance of R in the x-direction from a mouth. $i^{\mathrm{b}}/i_{(R)} = 0.81$ with $R = 300$ nm, and $i^{\mathrm{b}}/i_{(R)} = 1.00$ with $R = 700$ nm. Hence, the diffusion zones become completely 2D before R reaches 1 μm through coalescing. The concentration distribution steeply drops down to the local mouth concentration within the last 100–200 nm before entering into the pores (Fig. 5). Equation B-1 is thus

$$\frac{\partial C}{\partial x} = \frac{C^{\mathrm{b}} - C^{\mathrm{m}'}}{\delta\{1 - \exp[-N_{\mathrm{p}}\pi(R + r_{\mathrm{p}})^2]\}} \qquad \text{[B-2]}$$

List of Symbols

$C_{\mathrm{i}}^{\mathrm{b}}$	bulk concentration of species i, mol cm^{-3}
$C_{\mathrm{i}}^{\mathrm{m}}$	concentration of species i at mouths, mol cm^{-3}
$C_{\mathrm{i}}^{\mathrm{m}'}$	average concentration of species i at the template surface ($x = L'$), mol cm^{-3}
$C_{\mathrm{i}}^{\mathrm{s}}$	concentration of species i at the cathode surface, mol cm^{-3}
D_{i}	diffusion coefficient of species i, cm^2 s^{-1}
E	potential with respect to a reference electrode used, V
F	Faraday's constant, 96,500 C mol^{-1}
g	gravitational acceleration, 980 cm s^{-1}
$i_{\mathrm{i}}^{\mathrm{b}}$	partial current density of species i in the 2D diffusion layer outside the template, A cm^{-2}
$i_{\mathrm{i}}^{\mathrm{p}}$	partial current density of species i through pores, A cm^{-2}
L	template thickness, cm
L'	distance from the cathode surface to opening mouths, cm
m	mass of deposited metal, g
M	atomic weight of deposited metal, g mol^{-1}
N	sample number
N_{p}	number density of pores, cm^{-2}
pH^{b}	pH in bulk
pH^{m}	pH at mouths
pH^{s}	pH at cathode surface
P_{n}	probability to encounter the nth nearest neighbor for pores in the 2D plane of the template
Q	amount of electricity, C
r_{n}	distance to encounter the nth nearest neighbor for pores in the 2D plane of the template
r_{p}	pore radius, cm
R	diffusion field radius from mouths, cm
Ra^*	modified Rayleigh number
Sh	Sherwood number
t	time s
t_{p}	period from the beginning to the end of the second stage in deposition current transient, s
t^*	transference number of Ni^{2+} ions
z	valence number of ions

Greek

α	densification coefficient, cm^3 mol^{-1}
δ_{i}	2D diffusion layer thickness of species i measured from the template surface, cm
η	current efficiency, %
Θ	difference of $C_{\mathrm{Ni}^{2+}}^{\mathrm{b}}$ from $C_{\mathrm{Ni}^{2+}}^{\mathrm{m}'}$, mol cm^{-3}
μ	mean value, g, %
ν	kinematic viscosity, cm^2 s^{-1}
ρ	mass density of Ni, 8.90 g cm^{-3}
σ	standard deviation, g, %
σ^*	ratio of diffusion layer thickness of H^+ ions to that of Ni^{2+} ions

References

1. T. M. Whitney, J. S. Jiang, P. C. Searson, and C. L. Chien, *Science*, **261**, 1316 (1993).
2. K. Nielsch, R. B. Wehrspohn, J. Barthel, J. Kirschner, S. F. Fischer, H. Kronmüller, T. Schweinböck, D. Weiss, and U. Gösele, *J. Magn. Magn. Mater.*, **249**, 234 (2002).
3. L. Sun, Y. Hao, C.-L. Chien, and P. C. Searson, *IBM J. Res. Dev.*, **49**, 79 (2005).
4. H. Oshima, H. Kikuchi, H. Nakao, K. Itoh, T. Kamimura, T. Morikawa, K. Matsumoto, T. Umada, H. Tamura, K. Nishio, et al., *Appl. Phys. Lett.*, **91**, 022508 (2007).
5. C. W. Xu, H. Wang, P. K. Shen, and S. P. Jiang, *Adv. Mater.*, **19**, 4256 (2007).
6. X. Zhang, W. Lu, J. Da, H. Wang, D. Zhao, and P. A. Webley, *Chem. Commun. (Cambridge)*, **2009**, 195.
7. Z. Liu and P. C. Searson, *J. Phys. Chem. B*, **110**, 4318 (2006).
8. A. Andreu, J. W. Merkert, L. A. Lecaros, B. L. Broglin, J. T. Brazell, and M. El-Kouedi, *Sens. Actuators B*, **114**, 1116 (2006).
9. C. G. Zoski, N. Yang, P. He, L. Berdondini, and M. Koudelka-Hep, *Anal. Chem.*, **79**, 1474 (2007).
10. G. Tourillon, L. Pontonnier, J. P. Levy, and V. Langlais, *Electrochem. Solid-State Lett.*, **3**, 20 (1999).
11. J. Verbeeck, O. I. Lebedev, G. Van Tendeloo, L. Cagnon, C. Bougerol, and G. Tourillon, *J. Electrochem. Soc.*, **150**, E468 (2003).
12. W.-C. Yoo and J.-K. Lee, *Adv. Mater.*, **16**, 1097 (2004).
13. Q. Wang, G. Wang, X. Han, X. Wang, and J. G. Hou, *J. Phys. Chem. B*, **109**, 23326 (2005).
14. T. Chowdhury, D. P. Casey, and J. F. Rohan, *Electrochem. Commun.*, **11**, 1203 (2009).
15. Y. Fukunaka, M. Motoyama, Y. Konishi, and R. Ishii, *Electrochem. Solid-State Lett.*, **9**, C62 (2006).
16. D. M. Davis and E. J. Podlaha, *Electrochem. Solid-State Lett.*, **8**, D1 (2005).
17. L. Philippe and J. Michler, *Small*, **4**, 904 (2008).
18. H. Cao, L. Wang, Y. Qiu, Q. Wu, G. Wang, L. Zhang, and X. Liu, *ChemPhysChem*, **7**, 1500 (2006).
19. C.-C. Hu, K.-H. Chang, M.-C. Lin, and Y.-T. Wu, *Nano Lett.*, **6**, 2690 (2006).
20. M. Nishizawa, V. P. Menon, and C. R. Martin, *Science*, **268**, 700 (1995).
21. F. Q. Zhu, D. Fan, X. Zhu, J.-G. Zhu, R. C. Cammarate, and C.-L. Chien, *Adv. Mater.*, **16**, 2155 (2004).
22. C. J. Brumlik and C. R. Martin, *J. Am. Chem. Soc.*, **113**, 3174 (1991).
23. V. P. Menon and C. R. Martin, *Anal. Chem.*, **67**, 1920 (1995).
24. J. Bao, C. Tie, Z. Xu, Q. Zhou, D. Shen, and Q. Ma, *Adv. Mater.*, **13**, 1631 (2001).
25. N. Q. Minh, *J. Am. Ceram. Soc.*, **76**, 563 (1993).
26. S. Kang, P. C. Su, Y. L. Park, Y. Saito, and F. B. Prinz, *J. Electrochem. Soc.*, **153**, A554 (2006).
27. M. A. Peña, J. P. Gómez, and J. L. G. Fierro, *Appl. Catal., A*, **144**, 7 (1996).
28. P. Serp, M. Corrias, and P. Kalck, *Appl. Catal., A*, **253**, 337 (2003).
29. J. O'M. Bockris and E. C. Potter, *J. Chem. Phys.*, **20**, 614 (1952).
30. M. Motoyama, Y. Fukunaka, T. Sakka, and Y. H. Ogata, *J. Electrochem. Soc.*, **153**, C502 (2006).
31. Y. Konishi, M. Motoyama, H. Matsushima, Y. Fukunaka, R. Ishii, and Y. Ito, *J. Electroanal. Chem.*, **559**, 149 (2003).
32. M. Motoyama, Y. Fukunaka, T. Sakka, Y. H. Ogata, and S. Kikuchi, *J. Electroanal. Chem.*, **584**, 84 (2005).
33. A. K. Graham, *Electroplating Engineering Handbook*, p. xii, Van Nostrand Reinhold, New York (1972).
34. A. M. Alfantazi and A. Shakshouki, *J. Electrochem. Soc.*, **149**, C506 (2002).
35. C. R. Martin, M. Nishizawa, K. Jirage, M. Kang, and S. B. Lee, *Adv. Mater.*, **13**, 1351 (2001).
36. J. B. Edel and A. J. de Mello, *Nanofluidics: Nanoscience and Nanotechnology*, Royal Society of Chemistry, Cambridge, UK (2009).
37. Z. Li and B. C.-Y. Lu, *Chem. Eng. Sci.*, **56**, 2879 (2001).
38. C. E. Brennen, *Cavitation and Bubble Dynamics*, Oxford University Press, New York (1995).
39. Y. Fukunaka, K. Suzuki, A. Ueda, and Y. Kondo, *J. Electrochem. Soc.*, **136**, 1002 (1989).
40. Y. Fukunaka, T. Minegishi, N. Nishioka, and Y. Kondo, *J. Electrochem. Soc.*, **128**, 1274 (1981).

41. S. Valizadeh, J. M. George, P. Leisner, and L. Hultman, *Electrochim. Acta*, **47**, 865 (2001).
42. M. Avrami, *J. Chem. Phys.*, **7**, 1103 (1939); , **8**, 212 (1940); , **9**, 177 (1941).
43. B. Scharifker and G. Hills, *Electrochim. Acta*, **28**, 879 (1983).
44. B. R. Scharifker, *J. Electroanal. Chem.*, **240**, 61 (1988).
45. A. Milchev, W. S. Kruijt, M. Sluyters-Rehbach, and J. H. Sluyters, *J. Electroanal. Chem.*, **350**, 89 (1993).
46. C. Schönenberger, B. M. I. van der Zande, L. G. J. Fokkink, M. Henny, C. Schmid, M. Krüger, A. Bachtold, R. Huber, H. Birk, and U. Staufer, *J. Phys. Chem. B*, **101**, 5497 (1997).
47. C. Wagner, *J. Electrochem. Soc.*, **95**, 161 (1949).
48. C. R. Wilke, M. Eisenberg, and C. W. Tobias, *J. Electrochem. Soc.*, **100**, 513 (1953).
49. Y. Fukunaka, T. Yamamoto, and Y. Kondo, *Electrochim. Acta*, **34**, 1393 (1989).
50. Y. Fukunaka, K. Denpo, M. Iwata, K. Maruoka, and Y. Kondo, *J. Electrochem. Soc.*, **130**, 2492 (1983).
51. K. Denpo, T. Okumura, Y. Fukunaka, and Y. Kondo, *J. Electrochem. Soc.*, **132**, 1145 (1985).
52. M. Poubaix, *Atlas of Electrochemical Equilibria in Aqueous Solutions*, Pergamon, London (1966).
53. J. Horkans, *J. Electrochem. Soc.*, **126**, 1861 (1979).
54. J. P. Hoare, *J. Electrochem. Soc.*, **133**, 2491 (1986); , **134**, 3102 (1987).
55. M. Murthy, G. S. Nagarajan, J. W. Weidner, and J. W. Van Zee, *J. Electrochem. Soc.*, **143**, 2319 (1996).
56. H. Dahms and I. M. Croll, *J. Electrochem. Soc.*, **112**, 771 (1965).
57. S. Hessami and C. W. Tobias, *J. Electrochem. Soc.*, **136**, 3611 (1989).
58. J. K. Park and K. J. Lee, *J. Chem. Eng. Data*, **39**, 891 (1994).
59. H. Vogt, *J. Appl. Electrochem.*, **25**, 764 (1995).
60. W.-C. Tsai, C.-C. Wan, and Y.-Y. Wang, *J. Appl. Electrochem.*, **32**, 1371 (2002).
61. M. Motoyama, T. Sakka, Y. H. Ogata, and Y. Fukunaka, *Electrochim. Acta*, **53**, 205 (2007).
62. G. C. Han, B. Y. Zong, P. Luo, and Y. H. Wu, *J. Appl. Phys.*, **93**, 9202 (2003).
63. F. E. Atalay, H. Kaya, S. Atalay, and S. Tari, *J. Alloys Compd.*, **469**, 458 (2009).